

## Observing the reconnection region in a transequatorial loop system

Rui Liu<sup>1</sup>, Tong-Jiang Wang<sup>2</sup>, Jeongwoo Lee<sup>3</sup>, Guillermo Stenborg<sup>4</sup>, Chang Liu<sup>1</sup>,  
Sung-Hong Park<sup>1,5</sup> and Hai-Min Wang<sup>1</sup>

<sup>1</sup> Space Weather Research Laboratory, Center for Solar-Terrestrial Research, NJIT, Newark, NJ 07102, USA; [rui.liu@njit.edu](mailto:rui.liu@njit.edu)

<sup>2</sup> Catholic University of America and NASA Goddard Space Flight Center, Greenbelt, MD 20771, USA

<sup>3</sup> Department of Physics, NJIT, Newark, NJ 07102, USA

<sup>4</sup> Interferometrics, Inc. Herndon, VA 20171, USA

<sup>5</sup> Korea Astronomy and Space Science Institute, Daejeon 305-348, Republic of Korea

Received 2011 February 25; accepted 2011 June 9

**Abstract** A vertical current sheet is a crucial element in many flare/coronal mass ejection (CME) models. For the first time, Liu et al. reported a vertical current sheet directly imaged during the flare rising phase with the EUV Imaging Telescope (EIT) onboard the Solar and Heliospheric Observatory (*SOHO*). As a follow-up study, here we present the comprehensive analysis and detailed physical interpretation of the observation. The current sheet formed due to the gradual rise of a transequatorial loop system. As the loop legs approached each other, plasma flew at  $\sim 6 \text{ km s}^{-1}$  into a local area where a cusp-shaped flare loop subsequently formed and the current sheet was seen as a bright, collimated structure of global length ( $\geq 0.25 R_{\odot}$ ) and macroscopic width  $((5-10) \times 10^3 \text{ km})$ , extending from 50 Mm above the flaring loop to the border of the EIT field of view (FOV). The reconnection rate in terms of the Alfvén Mach number is estimated to be only 0.005–0.009, albeit a halo CME was accelerated from  $\sim 400 \text{ km s}^{-1}$  to  $\sim 1300 \text{ km s}^{-1}$  within the coronagraph FOV. Drifting pulsating structures at metric frequencies were recorded during the impulsive phase, implying tearing of the current sheet in the high corona. A radio Type III burst occurred when the current sheet was clearly seen in EUV, indicative of accelerated electrons beaming upward from the upper tip of the current sheet. A cusp-shaped dimming region was observed to be located above the post-flare arcade during the decay phase in EIT; both the arcade and the dimming expanded with time. With the Coronal Diagnostic Spectrometer (CDS) aboard *SOHO*, a clear signature of chromospheric evaporation was seen during the decay phase, i.e., the cusp-shaped dimming region was associated with plasma upflows detected with EUV hot emission lines, while the post-flare loop was associated with downflows detected with cold lines. This event provides a comprehensive view of the reconnection geometry and dynamics in the solar corona.

**Key words:** Sun: coronal mass ejections — Sun: flares — Sun: corona

## 1 INTRODUCTION

Magnetic energy is the only viable energy source to power eruptive phenomena in the solar corona (Forbes 2000), such as solar flares, eruptive prominences and coronal mass ejections (CMEs). Magnetic reconnection is a global topological restructuring of the magnetic field in a neutral region, such as neutral point, null point, current sheet, or quasi-separatrix layer, where a local decoupling between plasma and field makes possible the rapid dissipation of magnetic free energy in the highly conducting and force-free coronal environment (Priest & Forbes 2000). A vertical current sheet is generally expected to form when a closed magnetic structure is highly stretched due either to the shearing of its footpoints (e.g., Karpen et al. 1995), or to the catastrophic loss of equilibrium in a magnetic flux rope (e.g., Forbes & Priest 1995), or, in the classical “standard” flare model (Kopp & Pneuman 1976), to a rising filament above the magnetic polarity inversion line. The reconnection at this current sheet, on the one hand, breaks the field lines that serve to confine the closed magnetic structure, which consequently escapes as a CME and on the other hand, converts magnetic energy to plasma energy. The resultant intense heating creates growing flare loops in the corona and separating flare ribbons in the chromosphere. Accelerated electrons that spiral along magnetic fields down to the dense chromosphere are instantly stopped by ions/protons and emit hard X-rays (HXR). Heated by nonthermal electrons or by thermal conduction, chromospheric plasma “evaporates” into closed flux tubes formed in the reconnection process and emits soft X-rays (SXR; Fisher et al. 1985). Meanwhile, accelerated electrons interacting with magnetized plasmas excite various radio emissions (see the review by Aschwanden 2002).

Pieces of indirect evidence highly suggestive of reconnection in the corona have accumulated over decades of observations. These include candlelight flare loops implying an X-type or Y-type reconnection point above the detectable cusp (Tsuneta et al. 1992), high-temperature plasma along the field lines mapping to the tip of the cusp (Tsuneta 1996), loop shrinkage implying that newly reconnected field lines relax from the initial cusp shape to a more dipolar shape (Forbes & Acton 1996), an HXR source above the SXR looptop (e.g., Masuda et al. 1994) implying energy release above the flare loop, upward-moving plasmoid (Shibata et al. 1995) and supra-arcade downflow (McKenzie & Hudson 1999) implying reconnection outflows and horizontal converging motion at  $\sim 5 \text{ km s}^{-1}$  in EUV above a cusp-shaped SXR flare loop implying reconnection inflow (Yokoyama et al. 2001; Narukage & Shibata 2006). More recently, a coronal HXR source was observed to be located well above a cusp-shaped flare loop in the impulsive phase (Sui & Holman 2003), which is suggested to indicate the formation of a large-scale current sheet in between. The flare loop initially shrank and then grew outward at a speed of several kilometers per second, while the coronal source moved outward at  $\sim 300 \text{ km s}^{-1}$ , which is interpreted as the extension of the current sheet. Further investigations reveal that the descending motion of the flare looptop emission is often accompanied by the converging motion of the conjugate footpoints (e.g., Ji et al. 2006, 2007; Liu et al. 2009a,b; Joshi et al. 2009) and is followed by the conventional expansion of the flare loop system.

Considerable attention has also been given to a coaxial, bright ray feature that appears several hours after some CMEs, which is argued as evidence for the current sheet (Webb et al. 2003; Ko et al. 2003; Lin et al. 2005). Along the ray, bright blobs are often observed to flow away from the Sun, suggestive of reconnection outflows (Ko et al. 2003; Lin et al. 2005). A few post-CME rays were studied with UV spectra acquired at  $1.5\text{--}1.7 R_{\odot}$  (Ciaravella et al. 2002; Ko et al. 2003; Raymond et al. 2003; Bemporad et al. 2006; Ciaravella & Raymond 2008), in which the narrow emission of highly ionized ions indicates an unusually high temperature for the corona at this height. These physical and dynamical properties are generally consistent with the theoretical expectations for current sheets, except that there is a huge gap between the observed and the predicted thickness of the current sheet. The theory based on classical resistivity predicts that the sheet thickness is only on the order of a proton gyroradius (tens of meters in the corona; Lin et al. 2009), but the thickness of the post-CME rays is about  $10^5 \text{ km}$ . Turbulence may help to bridge the gap (Bemporad

2008), as the large-scale current sheet is subject to the tearing and coalescence instabilities as well as their combined dynamics (Priest & Forbes 2000). Alternatively, it was suggested to interpret the ray feature as a plasma sheet (Liu et al. 2009d), since it is comparable in width to the heliospheric plasma sheet where a much narrower heliospheric current sheet ( $(3-10) \times 10^3$  km) is embedded (Winterhalter et al. 1994). This is consistent with the recent high-resolution SXR observation of a post-CME ray feature in the low corona (Savage et al. 2010), whose average thickness is measured to be 4500 km. However, considering the long lifetime (from hours to days) of post-CME rays, a question stands out as to why their counterpart is rarely seen during CMEs, albeit the eruption-time current sheet is expected to be more dynamic and unstable.

For the first time, Liu et al. (2010a) reported a bright sheet structure distinctly above the cusp-shaped flaring loop, imaged during the flare rising phase in EUV. In this paper, we present the comprehensive analysis and detailed physical interpretation of the sheet structure, whose geometry and dynamics are highly suggestive of a Y-type current sheet (Sect. 2). Various signatures of the reconnection, including inflows, outflows, chromospheric evaporation and relevant radio emissions, are also presented in detail in Section 2. We will further discuss several aspects of the observation in Section 3 and summarize the results in Section 4.

## 2 OBSERVATION AND ANALYSIS

Transequatorial loops are an important element in Babcock's conceptual model of the solar magnetic cycle (Babcock 1961), reconnection of which helps to restore the poloidal field in preparation for a new cycle. Khan & Hudson (2000) identified the disappearance of transequatorial loops in close association with major flares and CMEs. Various studies confirmed that as a large-scale source region of CMEs, the flaring behavior of transequatorial loops is similar to that seen in active-region flares (e.g., Harra et al. 2003). The transequatorial loop system (TLS) studied here was connecting two active regions, NOAA Active Region 10652 in the northern hemisphere and AR 10653 in the southern hemisphere, the former of which is of  $\beta\gamma\delta$  type while the latter of  $\beta$  type (Fig. 1(a) and (d)). We are particularly interested in the eruption of the TLS on 2004 July 29 when the two active regions were located on the west limb.

In the subsections that follow, we introduce the instruments that are used in our study (Sect. 2.1). Before studying the 2004 July 29 eruption, we briefly investigate the two previous eruptions occurring on July 23 and 25, which are homologous to the limb event of interest (Sect. 2.2). In Section 2.3, we study in detail the dynamics and structure of the reconnection region produced in the 2004 July 29 eruption. In Section 2.4, we exploit the observed radio signatures to derive some physical parameters of the reconnection region. In Section 2.5, we explore the nature of a cusp-shaped dimming region above the post-flare arcade. Some of the results in Section 2.3–Section 2.5 have been briefly introduced in the Letter by Liu et al. (2010a) and here a comprehensive analysis is presented.

### 2.1 Instruments

The eruption of the TLS on 2004 July 29 in the low corona was observed both by the EUV Imaging Telescope (EIT; Delaboudinière et al. 1995) onboard the Solar and Heliospheric Observatory (*SOHO*) and by the Transition Region and Coronal Explorer (*TRACE*; Handy et al. 1999). The ensuing CME was observed by the Large Angle and Spectrometric Coronagraph (LASCO; Brueckner et al. 1995) onboard *SOHO*, which consists of two operational optical systems, C2 ( $2.2-6.0 R_{\odot}$ ) and C3 ( $4-32 R_{\odot}$ ). Relevant radio emissions were recorded by the Green Bank Solar Radio Burst Spectrometer (GBSRBS<sup>1</sup>) on the ground and the WAVES instrument onboard the WIND spacecraft (Bougeret et al. 1995).

---

<sup>1</sup> <http://gsrbs.nrao.edu/>

EIT has a  $45' \times 45'$  FOV with a pixel scale of  $2.6'' \text{ pixel}^{-1}$ . It takes full-disk images at a 12-min cadence in the 195 Å channel (Fe 12;  $1.6 \times 10^6$  K). The TLS was only partially covered by the *TRACE* 195 Å channel, whose FOV ( $8.5' \times 8.5'$ ) was centered on AR 10652 till 15:40 UT on 2004 July 29, with a pixel scale of  $0.5'' \text{ pixel}^{-1}$  and a time cadence of 40 s. It is noteworthy that both the EIT and *TRACE* 195 Å channels are also sensitive to high-temperature flare plasma because of the presence of the Fe 24 resonance line ( $\lambda 192$ ;  $2 \times 10^7$  K), which is negligible in the quiet region but dominates in the flaring region (Tripathi et al. 2006). In addition to the standard processing using the SolarSoftWare (SSW) procedure, `EIT_PREP`, we have further processed the EIT 195 Å images by removing the instrumental stray-light background and by enhancing the fine coronal structures with a wavelet method (Stenborg et al. 2008). When overlaying high-resolution *TRACE* images on the enhanced EIT images taken at approximately the same time (see Sect. 2.3), one can see that the algorithm enhances the coronal features at very high fidelity.

The Coronal Diagnostic Spectrometer (CDS; Harrison et al. 1995) onboard *SOHO* was pointing at AR 10652 from 13:32 to 21:41 UT on 2004 July 29, including four raster scans. Despite the limited FOV of the raster images ( $4' \times 4'$ ), CDS captured the northern leg of the post-flare loop. We will concentrate on the first raster scan (13:32–15:32 UT), when a cusp-shaped dimming region above the post-flare arcade was seen in EIT 195 Å. Brosius (2006) studied the post-flare arcade using CDS data obtained during the third raster scan (17:37–19:38 UT).

## 2.2 Homologous Eruptions

The TLS erupted three times during its disk passage, resulting in three halo CMEs. The first eruption occurred at about 17:36 UT on 2004 July 23, initiating with a jet associated with a flare from AR 10652 in the north (N08W08; Fig. 1(b)), while AR 10653 in the south (S12W09) appeared to react passively during the eruption. The same pattern is repeated in the second (2004 July 25 13:48 UT) and third (2004 July 29 12:00 UT) eruptions. This suggests that AR 10652 was the major driver of the eruptions, as evidenced by a much larger helicity injection rate in AR 10652 than that in AR 10653 (see the appendix for the calculation method). On the other hand, the unsigned fluxes<sup>2</sup> integrated over both active regions were more or less constant during their disk passage (Fig. 2(c)), indicating that the helicity injection was mainly driven by photospheric flows rather than by flux emergence.

The middle panels of Figure 1 show the TLS prior to each eruption and the bottom panels the post-eruptive arcade. The east-west extent of the post-eruptive arcade is measured to be  $(7 \pm 1) \times 10^9$  cm near the disk center (Fig. 1(c)), which provides an estimation of the line-of-sight depth for the limb observation on 2004 July 29. Based on the disk observation, we can also infer that the TLS (Fig. 1(g)) as well as the post-eruptive arcade (Fig. 1(h)) on July 29 was oriented predominantly in the north-south direction, with the northern footpoints slightly behind the southern ones (about  $10^\circ$ ). Hence this configuration is favorable for the comparison with the two-dimensional standard flare model.

The post-flare loops of the TLS (but not the TLS itself) can be reasonably reconstructed by linear-force-free field extrapolation (Nakagawa & Raadu 1972; Seehafer 1978), i.e.,  $\nabla \times \mathbf{B} = \alpha \mathbf{B}$ , with  $\alpha \approx 1.3 \times 10^{-8} \text{ m}^{-1}$ . The red lines in Figure 1 (a) and (c) show the extrapolated field lines that display similar morphology to the post-flare loops on July 24 (Fig. 1(c)). Being rotated rigidly towards the limb with the Sun, these field lines still bear similarities to the post-flare loops on July 25 and 29 (Fig. 1(f) and (h)). The field strength at the looptop is estimated to be  $21 \pm 3$  G, when averaged over the six extrapolated field lines as shown in Figure 1. The corresponding Alfvén speed at the post-flare looptop,  $V_A = 2.18 \times 10^{11} B / \sqrt{\mu n_e} \approx 6 \times 10^7 \text{ cm s}^{-1}$ , where  $\mu = 1.27$  is the molecular weight in the corona and  $n_e \approx 5 \times 10^9 \text{ cm}^{-3}$  is estimated with the density-sensitive Si 10

<sup>2</sup> The sum of absolute values of both positive and negative fluxes.

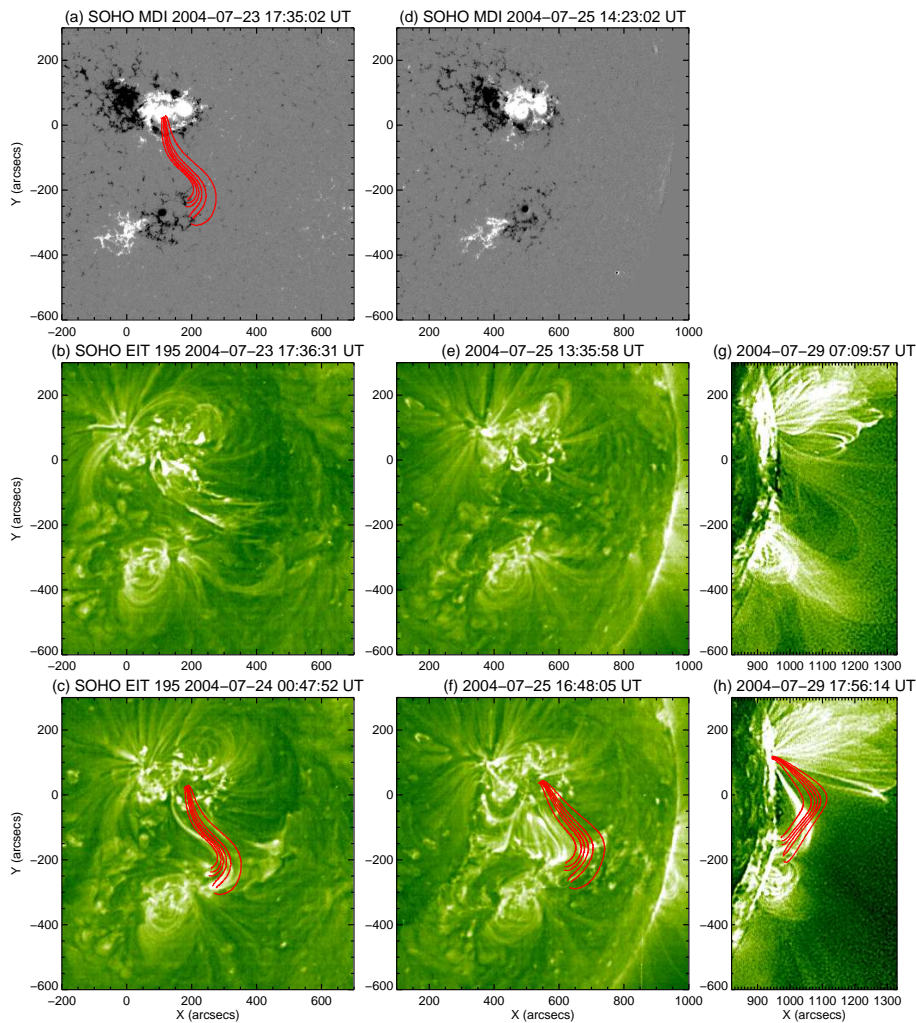


**Fig. 1** Eruptions of the transequatorial loop system during its disk passage. *Top row*: MDI magnetograms; *Middle row*: transequatorial loops prior to the eruption in EIT 195 Å; *Bottom row*: post-eruptive arcades in EIT 195 Å. In Panels (a) and (c), the red loops are field lines obtained via a linear force-free field extrapolation with  $\alpha = 1.3 \times 10^{-2}$  Mm. In Panels (f) and (h), these loops are rigidly rotated to match the post-eruptive arcades in later eruptions.

line pair ( $\lambda 347.4/356.0$ ; see Sect. 2.5). We note that, however, the planar boundary adopted in the extrapolation for such a large FOV may result in large uncertainties.

### 2.3 Dynamics & Structure of the Reconnection Region

The TLS erupted at about 12:00 UT on 2004 July 29, but can be clearly seen to slowly rise since as early as 2004 July 28 21:12 UT, apparently evolving from the post-eruptive arcade on 2004 July 25 (Fig. 1(f); see also Liu et al. 2010b). Due presumably to the footpoints being tied to the extremely dense photosphere, the two legs of the transequatorial loop approached each other with the rise. This

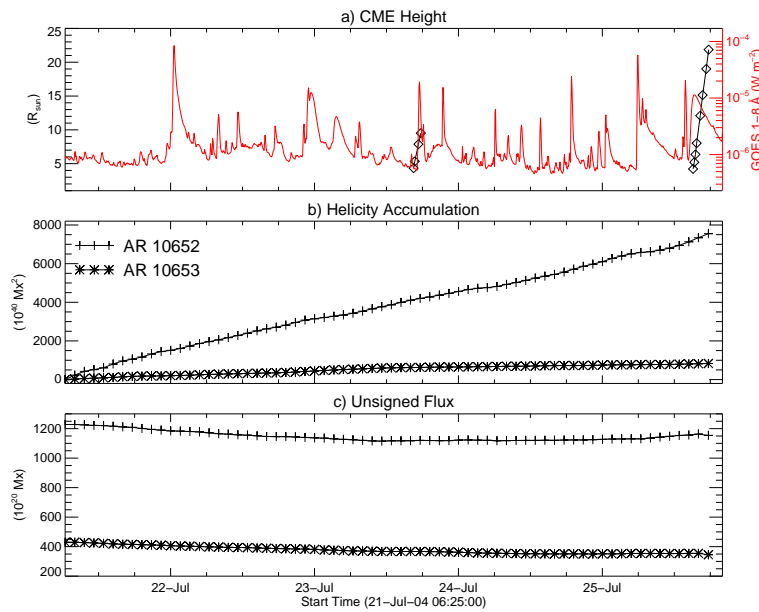


**Fig. 2** Evolution of the photospheric fields in ARs 10652 and 10653 during their disk passage (within  $45^\circ$  from the central meridian). (a) Height-time revolution of the two halo CMEs, scaled by the  $y$ -axis on the left and GOES 1–8 Å flux, scaled by the  $y$ -axis on the right; (b) amount of helicity accumulation; (c) unsigned flux.

is evidenced by the sequential EIT 195 Å images in Figure 3(a)–(c) showing that the “waist” of the TLS became thinner with time. By placing a slit across the waist (Fig. 3(a)–(f)) and then putting all the resultant strips in chronological order (Fig. 4(e)), one can see that initially the waist converged at  $\sim 1 \text{ km s}^{-1}$  and then the speed suddenly increased to  $\sim 6 \text{ km s}^{-1}$  from 11:08 till 12:20 UT when a cusp-shaped flare loop formed (Fig. 3(d)). From 11:30 to 13:30 UT, GBSRBS recorded drifting pulsating structures (DPSs) at metric frequencies (Fig. 4(c)), suggestive of the tearing of a current sheet and the upward movement of the resultant plasmoids (see Sect. 2.4).

At 12:20 UT (Fig. 3(d)), a bright, collimated feature can be seen to extend for 170 Mm ( $0.25 R_\odot$ ) from well above a cusp-shaped flaring loop to the border of the EIT FOV ( $1.5 R_\odot$ ), presumably resulting from the reconnection of the approaching loop legs. This is similar in morphology to the Y-type current sheet in the standard flare model (Kopp & Pneuman 1976). At approximately the same time (12:23 UT), *WIND WAVES* recorded a Type III burst (Fig. 4(b)), which we interpret as evidence for relativistic electrons beaming upward from the upper tip of the current sheet. During the flare rising phase, *TRACE* observed both downward and upward propagating features along the northern leg of the flare loop at an average speed of  $\sim 200 \text{ km s}^{-1}$  (or  $\sim 100 \text{ km s}^{-1}$  in the gravitational direction; see Figure 4(d) and the top and middle panels of Figure 5). The upward propagating feature was probably associated with hot upflowing plasma evaporating from the chromosphere and the downward propagating feature with cooled plasma falling back down the flare loop. Clear signatures of chromospheric evaporation were also detected by CDS during the decay phase (see Sect. 2.5).

We refer to the lower tip of the current sheet (Fig. 3(d)) and later, the cusp point (Fig. 3(e) and (f)), as the (inverse) Y-point. Marked by a ‘×’ symbol in Figure 3, the Y-point is determined as the average location from multiple measurements, whose standard deviation is taken as the error bar in

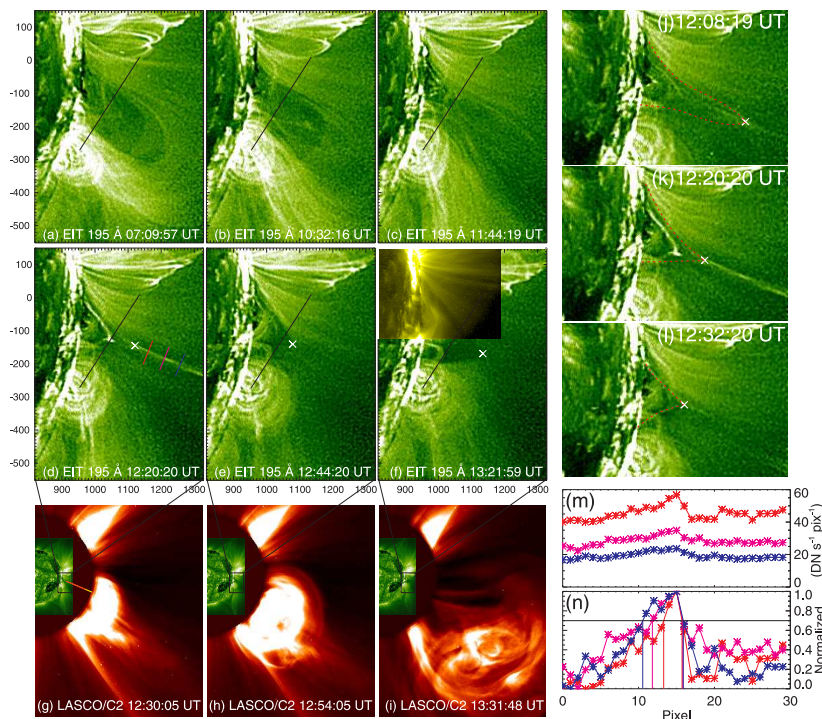


**Fig. 3** Expansion and subsequent eruption of the TLS observed in EIT and LASCO C2. EIT images are enhanced with a wavelet technique (Stenborg et al. 2008). In Panel (f) the EIT 195 Å image is overlaid by a *TRACE* 195 Å image taken at the same time. Panels (j–l) show detailed evolution of the reconnecting current sheet, whose lower-tip is marked by a ‘x’ symbol. Based on observed coronal structures, field lines that are assumed to connect the lower tip of the current sheet to the solar surface are delineated in red dashed lines. Panels (m) and (n) show intensity distribution along the slits in Panel (d). The line colors correspond to the colors of different slits. An animation of EIT images overlaid by corresponding *TRACE* images is available at <http://harp.njit.edu/~ruiliu/download/preprint/fig3.mp4>.

Figure 4(d). At 12:20 UT (Fig. 3(d)), the lower tip of the current sheet was clearly located above the flare looptop by about 50 Mm ( $\sim 70''$ ) and the height ratio between the Y-point and the flare looptop is about 1.6. The geometry agrees with that obtained by an independent study of electron time of flight (Aschwanden et al. 1996). To measure the sheet thickness, we put three slits ( $30 \times 3$  pixels; in red, purple and blue, respectively) perpendicularly across the sheet (Fig. 3(d)). After “rebinning” the slits to  $30 \times 1$  pixels, we plot the intensity distribution along each slit in Figure 3(m). One can see that the sheet generally spans about 3–5 EIT pixels. In the normalized plot (Fig. 3(n)), we choose a bar of 0.7, which is above all the “side lobes” and calculate the width of the “central lobe” above the bar via interpolation, which gives 2.4, 4.0 and 5.3 pixels for the red, purple and blue slits, respectively. It may appear that the sheet thickness increases with height, but with the recorded counts and the contrast decreasing with height, the uncertainty of the measurement is also larger for the slit at higher altitude. The sheet thickness is about  $(5\text{--}10) \times 10^3$  km, which is an order of magnitude thinner than the width ( $10^5$  km) of the post-CME high-temperature region (Fe 18) measured with the *SOHO* UVCS slits (e.g., Ciaravella et al. 2002; Ko et al. 2003; Ciaravella & Raymond 2008), but is in agreement with the recent high-resolution observation of a post-CME ray feature in the low corona (Savage et al. 2010). The thickness also matches the width ( $\sim 4 \times 10^3$  km) of high-speed outflows of hot plasma

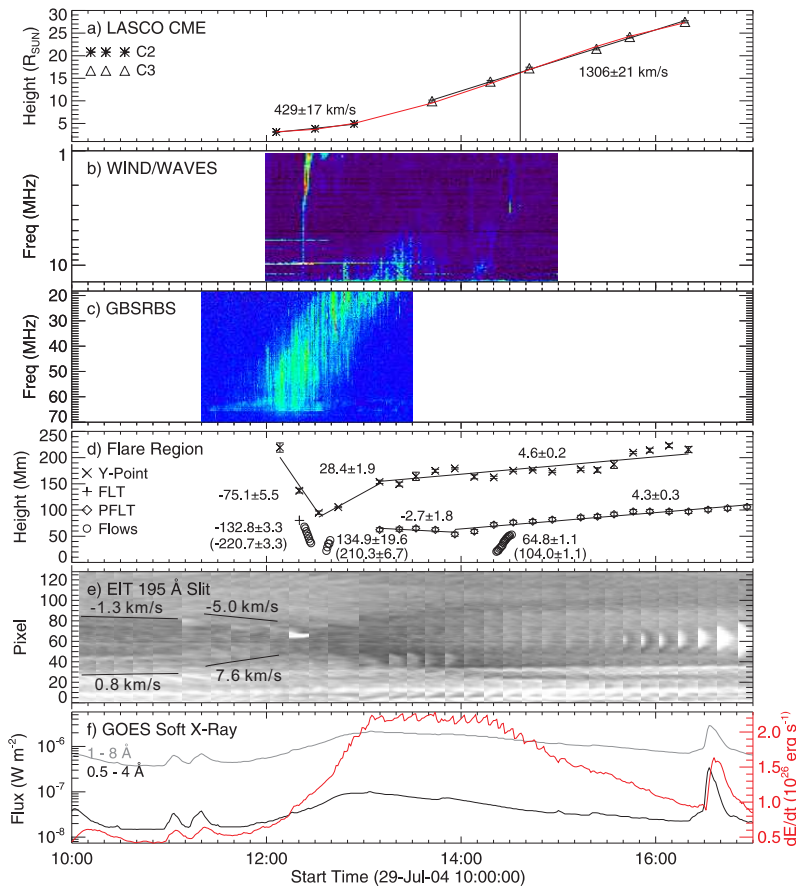


**Fig. 4** Dynamic evolution of the reconnection region. From top to bottom, (a) height-time profile of the LASCO CME; (b) *WIND WAVES* spectrogram showing a Type III burst; (c) GBSRBS spectrogram showing DPSs; (d) height-time evolution of the Y-point (‘×’), the flare looptop (FLT; ‘+’), the post-flare looptop (PFLT; diamond) and the propagating features observed by *TRACE* (circle); (e) chronological observation of the transequatorial loop through the slit as indicated in Figure 3(a)–(f); and (f) *GOES* SXR lightcurves, scaled by the  $y$ -axis on the left; and the corresponding radiative energy loss rate (in  $10^{26}$  erg  $s^{-1}$ ), scaled by the  $y$ -axis on the right. In Panel (d), speeds obtained by linear fits in  $\text{km s}^{-1}$  are displayed by the side of the corresponding height measurements; numbers in brackets are the projected speeds for *TRACE* propagating features.

near a reconnection site, detected in EUV spectra (Wang et al. 2007). Considering projection effects due to a small tilting angle between the normal to the flare-loop plane and the line of sight (about  $10^\circ$ ; Sect. 2.2), the “real” thickness should be smaller.

From 12:08 to 12:32 UT, the Y-point descended toward the solar surface from 219 Mm to 94 Mm at an average speed of  $75 \text{ km s}^{-1}$  (Fig. 4(d)), which is reminiscent of the downward motion of the looptop emission during the flare rising phase (Sui & Holman 2003; Sui et al. 2004; Liu et al. 2004; Veronig et al. 2006; Shen et al. 2008; Liu et al. 2008). Coronal features suggestive of field lines that connect the Y-point to the solar surface are delineated in red dashed lines in Figure 3(j–l), from which a shrinking trend in the flare loop can also be seen. The observed current sheet and the cusp-shaped flaring loop at 12:20 UT is very likely due to the Fe 24 emission at 20 MK. Both

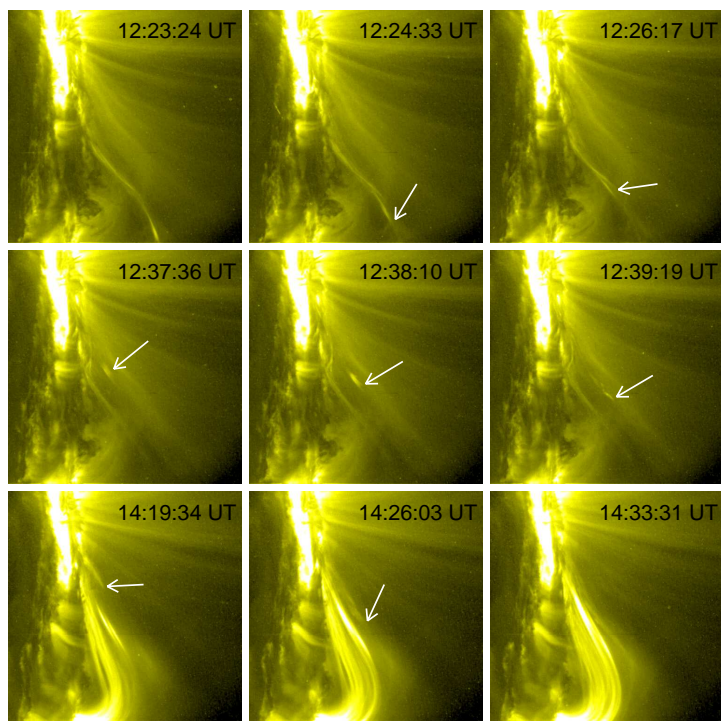


**Fig. 5** Propagating features observed along the *TRACE* flare loop.

faded out after the temporary appearance in the narrow  $195 \text{ \AA}$  filter, presumably due to cooling. The flare loop reappeared at 13:09 UT, assuming a more relaxed shape (e.g., Fig. 3(f)). Its apex was located at a lower altitude by about 17 Mm, indicating an average shrinkage speed of  $5.8 \text{ km s}^{-1}$ , similar to the results obtained by Forbes & Acton (1996). Obviously, the cusp-shaped flare loop (Fig. 3(d)) cooled and relaxed into the “post-flare loop” (Fig. 3(f)). In contrast, the bright current sheet never reappeared, probably maintaining a relatively high temperature. From 12:44 UT onward, an emission-depressed, cusp-shaped region appeared above the post-flare arcade (see Fig. 3(e)–(f)). Both structures expanded and rose with time, as clearly demonstrated in Figure 4(e); accordingly the Y-point, now identified with the cusp point, ascended at an average speed of  $28 \text{ km s}^{-1}$  till 13:09 UT and then at an average speed of  $4.6 \text{ km s}^{-1}$  till 16:20 UT (Fig. 4(d)), after which the cusp-shaped dimming became hardly discernible. The average height difference between the Y-point and the post-flare looptop is  $102 \pm 13 \text{ Mm}$  and the ratio of these two heights is  $2.3 \pm 0.3$ .

Initially, the post-flare looptop kept descending at an average speed of  $2.7 \text{ km s}^{-1}$  from 13:09 till 13:56 UT and then it underwent an apparent ascending motion at  $4.5 \text{ km s}^{-1}$  (Fig. 4(d)). In high-cadence, high-resolution *TRACE* images (also see the animation accompanying Fig. 3), one can clearly see the successive illumination of loops at higher and higher altitudes, which is observed as the apparent expansion of the post-eruptive arcade in low-cadence, low-resolution EIT images. The bottom panels of Figure 5 demonstrate the formation of one of the post-flare loops, in which a bright jet-like feature shot upward from the solar surface along a loop-shaped trajectory, with an average speed of  $104 \text{ km s}^{-1}$  (or  $65 \text{ km s}^{-1}$  in the gravitational direction; Fig. 4(d)). The jet decelerated at  $-54 \pm 7 \text{ m s}^{-2}$  (or,  $-26 \pm 7 \text{ m s}^{-2}$  in the gravitational direction,  $\sim 1/10 g_{\odot}$ ) with a second-order polynomial fit. We interpret the jet as the evaporated chromospheric plasma filling the flare loops (Antonucci et al. 1999). The jet speed is comparable to those of the upflows which occurred during the decay phase detected with SXR spectroscopy (e.g., Zarro & Lemen 1988, see also Sect. 2.5).

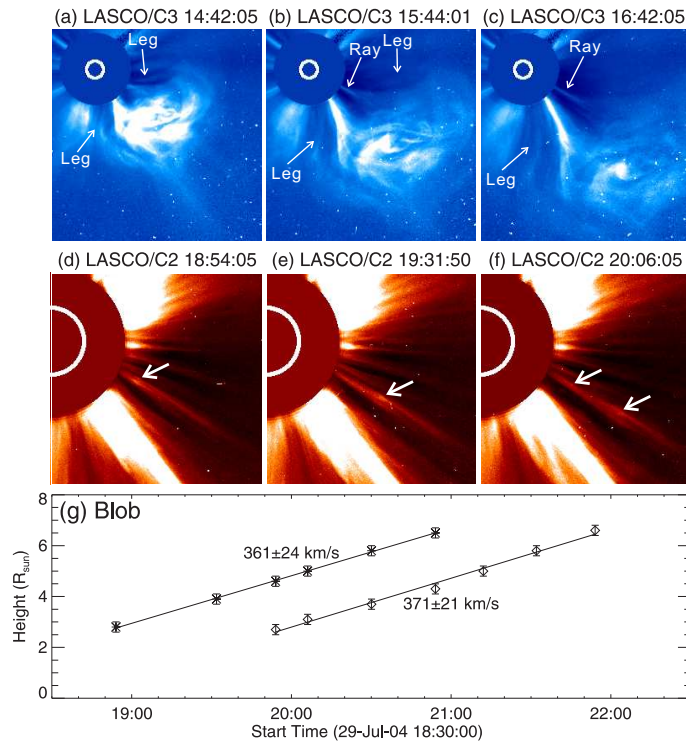


**Fig. 6** Post-CME Ray observed in LASCO in relation to the cusp-shaped dimming in EIT 195 Å. Panels (a)–(c) show the ray feature observed in LASCO C3. Panels (d)–(f) show the blobs moving outward along the post-CME ray in LASCO C2. Panel (g) shows the height-time evolution of two blobs, with a linear speed of  $\sim 360$  km s $^{-1}$  and  $\sim 370$  km s $^{-1}$ , respectively.

Despite the low contrast, from the cusp-shaped dimming one can still get a sense of the orientation of the current sheet, which appears to slowly rotate clockwise in the plane-of-sky projection (Fig. 3(d)–(f)). The current sheet was apparently aligned with a post-CME ray feature observed in LASCO (Fig. 6(b)–(f)), which was visible from 14:54 UT onward in LASCO C2. The ray was located between two CME legs, as can be seen in LASCO C3 (Fig. 6(a)–(c)) and rapidly fanned out above its upper tip (Fig. 6(b)–(c)) similarly to the vertical current sheet in the model (e.g., Lin & Forbes 2000) as well as in the simulation (e.g., Linker et al. 2003). Two blobs separated by about  $1.9 R_{\odot}$  were observed to move outward along the ray, implying the ejection of plasmoids (Fig. 6(d)–(f)), with a linear speed of  $\sim 360$  km s $^{-1}$  and  $\sim 370$  km s $^{-1}$ , respectively (Fig. 6(g)).

## 2.4 Radio Observation & Implication

### 2.4.1 Type III burst

The Type III burst was observed at the same time when the current sheet and the cusp-shaped flaring loop were clearly visible in EIT 195 Å at 12:20 UT (Fig. 3(d)). It can be seen to drift toward lower frequencies from the highest frequency, 13.8 MHz, of the 1-min averaged *WIND* WAVES spectrogram (Fig. 4(b)), but was invisible in the GBSRBS spectrogram in the 18.3–70.0 MHz frequency range (see Fig. 4(c)), from which the starting frequency of the Type III burst is inferred, i.e.,  $13.8 \text{ MHz} \leq f < 18.3 \text{ MHz}$ , where  $f = (n_e e^2 / \pi m_e)^{1/2} \approx 8980 \sqrt{n_e}$  Hz is the plasma frequency.

Hence the corresponding electron density,  $n_e$ , is in the range of  $(2.36\text{--}4.15) \times 10^6 \text{ cm}^{-3}$ . Adopting the density profile known as the Baumbach-Allen formula (Cox 2001),

$$n_e(R) = 10^8 \left[ 2.99 \left( \frac{R}{R_\odot} \right)^{-16} + 1.55 \left( \frac{R}{R_\odot} \right)^{-6} + 0.036 \left( \frac{R}{R_\odot} \right)^{-\frac{3}{2}} \right],$$

one obtains that  $1.95 R_\odot < R \leq 2.22 R_\odot$ , which we interpret as the heliocentric distance of the upper tip of the Y-type current sheet. The orientation of the current sheet in the EIT 195 Å image deviates from the radial direction by  $15^\circ$ . The heliocentric distance of the lower tip of the current sheet,  $r$ , is directly measured to be  $1.19 R_\odot$ , hence the length of the current sheet,  $L$ , can be calculated from  $L = r \cos \alpha + \sqrt{r^2(\cos^2 \alpha - 1) + R^2}$ , where  $\alpha = 165^\circ$ . The result is  $0.78 R_\odot < L \leq 1.05 R_\odot$ . The lower and upper bounds of  $L$  are indicated by a red and a yellow lines in Figure 3(g), respectively. From the EIT image (Fig. 3(d)) we know that  $L \geq 0.25 R_\odot \approx 170 \text{ Mm}$ .

#### 2.4.2 Drifting pulsating structures

It is known that DPSs are a series of quasi-periodic, Type III-like pulses observed in radio spectrograms, usually in the decimetric range 0.6 – 2 GHz. As a whole, DPSs often slowly drift towards higher or lower frequencies at a typical rate of  $-20 - 20 \text{ MHz s}^{-1}$  (Bárta et al. 2008). The clear association between DPSs and moving X-ray sources (e.g. Kliem et al. 2000; Kundu et al. 2001; Khan et al. 2002) suggests that DPSs are generated when plasmoids (magnetic islands) are formed in the magnetic reconnection process. MHD simulations (e.g. Kliem et al. 2000; Karlický & Bárta 2007; Bárta et al. 2008) show that the reconnection is dominated by a multiple tearing of the current sheet and the subsequent coalescence of plasmoids, known as the bursty regime of magnetic reconnection. In this scenario, electrons are accelerated and trapped as the plasmoids contract and mutually interact, probably in a classic Fermi manner (Drake et al. 2006), which generate the individual pulses of DPSs; the motion of the plasmoids in the inhomogeneous solar atmosphere results in the global drift of DPSs.

Thus, the fact that the current sheet and the DPSs were simultaneously observed in the event studied here implies that the current sheet must be fragmented at smaller scales although it appears to be a coherent structure in EIT and that the energy is redistributed and dissipated at smaller scales via MHD turbulent cascade than the scale at which it is supplied via plasma inflow.

Since the DPSs in our study were observed in the metric range of tens of MHz (Fig. 4(c)), it suggests that the plasmoids were formed in the very high corona. As the plasmoids moved outward, the DPSs drifted from 65 MHz to 18 MHz within about 45 min, i.e., at about  $-0.02 \text{ MHz s}^{-1}$ . Because the plasma density inside the plasmoids must decrease slower than the ambient atmosphere, the global drift rate gives the lower limit to the plasmoid speed. Again, exploiting the Baumbach-Allen formula, we estimate that the plasmoids moved upward at an average speed of  $180 \text{ km s}^{-1}$ . According to the Lin & Forbes (2000) model, the upper tip of the current sheet rises at a rate that is about half of the flux rope speed. In this case, if the plasmoid speed is assumed to be equivalent to that of the upper tip of the current sheet, the flux-rope speed would be  $\geq 360 \text{ km s}^{-1}$ , which surprisingly matches the CME speed ( $\sim 400 \text{ km s}^{-1}$ ) at the time of the DPS observation (Fig. 4).

### 2.5 Cusp-Shaped Dimming

The cusp-shaped dimming (see Fig. 3(e)–(f), also Fig. 4(e)) was seen as a dark region filling the region between the post-flare loop and the Y-type separatrix in EIT 195 Å (Fe 12;  $1.5 \times 10^6 \text{ K}$ ) and can also be seen in EIT 171 Å (Fe IX/X;  $1.3 \times 10^6 \text{ K}$ ) at 12:56 UT and 304 Å (He 2;  $8 \times 10^4 \text{ K}$ ) at 13:15 UT, but is not quite discernible in 284 Å (Fe 15;  $2 \times 10^6 \text{ K}$ ) at 13:02 UT. By overlaying the CDS raster images (Figs. 7 and 8) on the EIT 195 Å image (Fig. 9(d)), one can see that the EIT

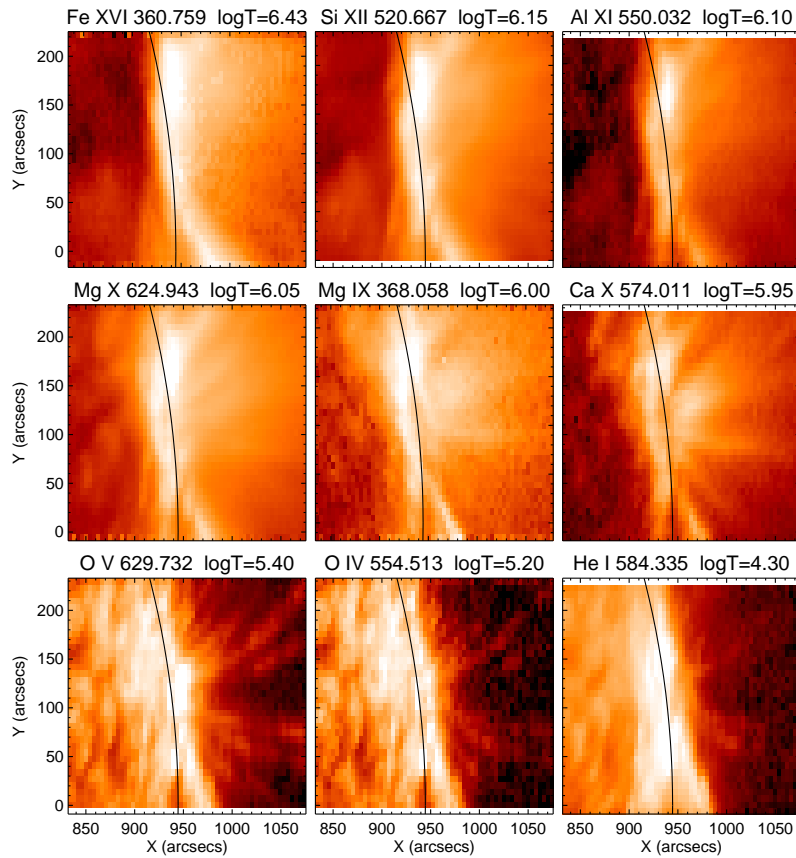


**Fig. 7** CDS raster images for different EUV lines obtained from multi-Gaussian fitting. Images are displayed in logarithm scale.

dimming that is located above the post-flare loop is bright in emission in hot CDS lines, such as Fe 16 ( $\lambda 360.8$ ;  $\log T = 6.43$ ) and Si 12 ( $\lambda 520.7$ ;  $\log T = 6.15$ ), while remaining dark in cool lines, such as O 5 ( $\lambda 629.7$ ;  $\log T = 5.40$ ), O 4 ( $\lambda 554.5$ ;  $\log T = 5.20$ ) and He 1 ( $\lambda 584.3$ ;  $\log T = 4.30$ ). This clearly demonstrates that hot loops are located above cool ones, hence we relate the EIT cusp-shaped dimming to SXR cusp-shaped flare loops that are often observed in long-duration events (e.g., Tsuneta et al. 1992; Tsuneta 1996) and we interpret it as a site of newly reconnected flux tubes. From the electron density map (Fig. 10) obtained from the Si 10 intensity ratio ( $\lambda 347.4/356.0$ ;  $\log T = 6.10$ ) with the CHIANTI atomic database (Dere et al. 1997, Version 6), one can see that the density of plasma at about 1.3 MK is low at the cusp-shaped region, which accounts for the dimming observed in EIT.

We fit the spectra from each CDS pixel with a broadened Gaussian profile and derive maps of relative Doppler velocities with respect to the average centroid wavelength, as CDS does not provide an absolute wavelength scale. Since regions above the limb appear brighter in hot lines and those on the disk appear brighter in cold lines, we limit our analysis to the area within which the intensities are above  $20 \text{ erg s}^{-1} \text{ cm}^{-2} \text{ sr}^{-1}$  for the hot lines (Ca 10, Mg 9, Mg 10, Al 11, Si 12 and Fe 16) and above  $100 \text{ erg s}^{-1} \text{ cm}^{-2} \text{ sr}^{-1}$  for the cool lines (He 1, O 4 and O 5). The obtained velocity maps show that Doppler redshifts dominate in the cusp-shaped region in hot lines, while blueshifts dominate in

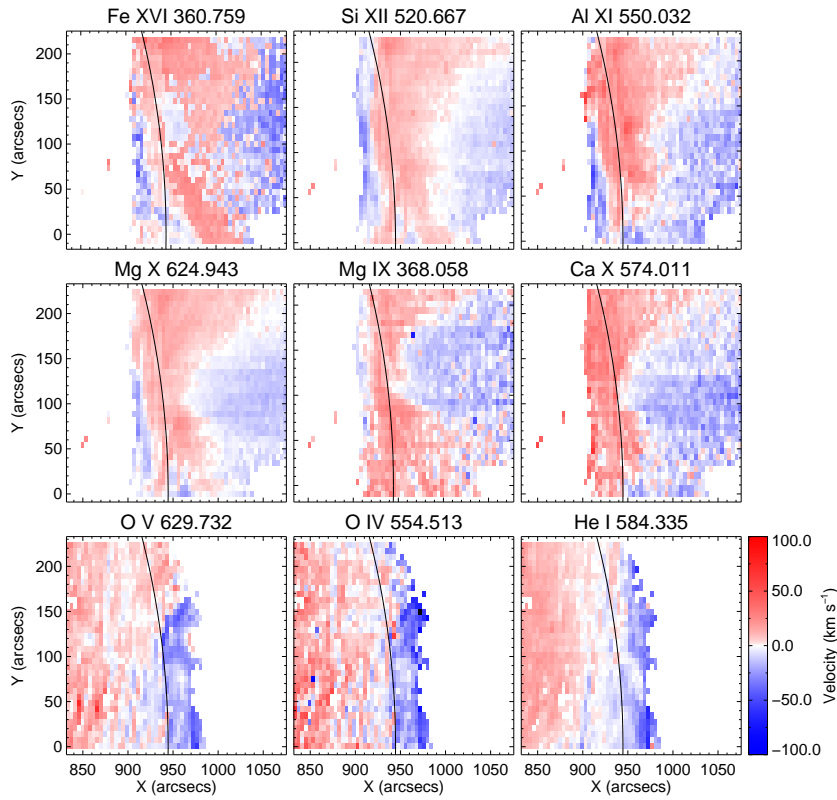


**Fig. 8** CDS velocity maps obtained from the EUV lines in Fig. 7.

the post-flare arcade in cool lines (Figs. 8 and 9(d)). This is because the flare-loop plane is tilted eastward by about  $10^\circ$  (Sect. 2.2), hence upflows of evaporating hot plasma along the northern leg bear a velocity component away from the observer (redshift), while downflows of precipitating cool plasma have a velocity component toward the observer (blueshift). This is illustrated in a schematic diagram in Figure 9(a). For Fe 16, the redshift gives an average speed of  $19 \pm 4 \text{ km s}^{-1}$ ; and for O 5, the blueshift gives an average speed of  $24 \pm 10 \text{ km s}^{-1}$ . We corrected the projection effect by taking into account the tilt angle of the flare-loop plane and by assuming an angle of  $45^\circ$  ( $30^\circ$ ) for the leg of the cusp region (post-flare loop) with respect to the local surface. This gives an upflow (downflow) speed of  $150$  ( $-160$ )  $\text{km s}^{-1}$ , which is comparable to the speeds of the propagating features observed in *TRACE* (Fig. 4(d) and Fig. 5).

### 3 DISCUSSION

#### 3.1 Detection of the Current Sheet

If the vertical current sheet is a plate of thickness  $d$  and depth  $D$  (Fig. 9(a–b)), then its detection depends very much on the line-of-sight depth  $D'$  across the plate. Define  $\theta$  as the angle between the line of sight and plate plane, then

$$D' = \begin{cases} D/\cos\theta & (\tan\theta \leq d/D) \\ d/\sin\theta & (\tan\theta > d/D) \end{cases}.$$

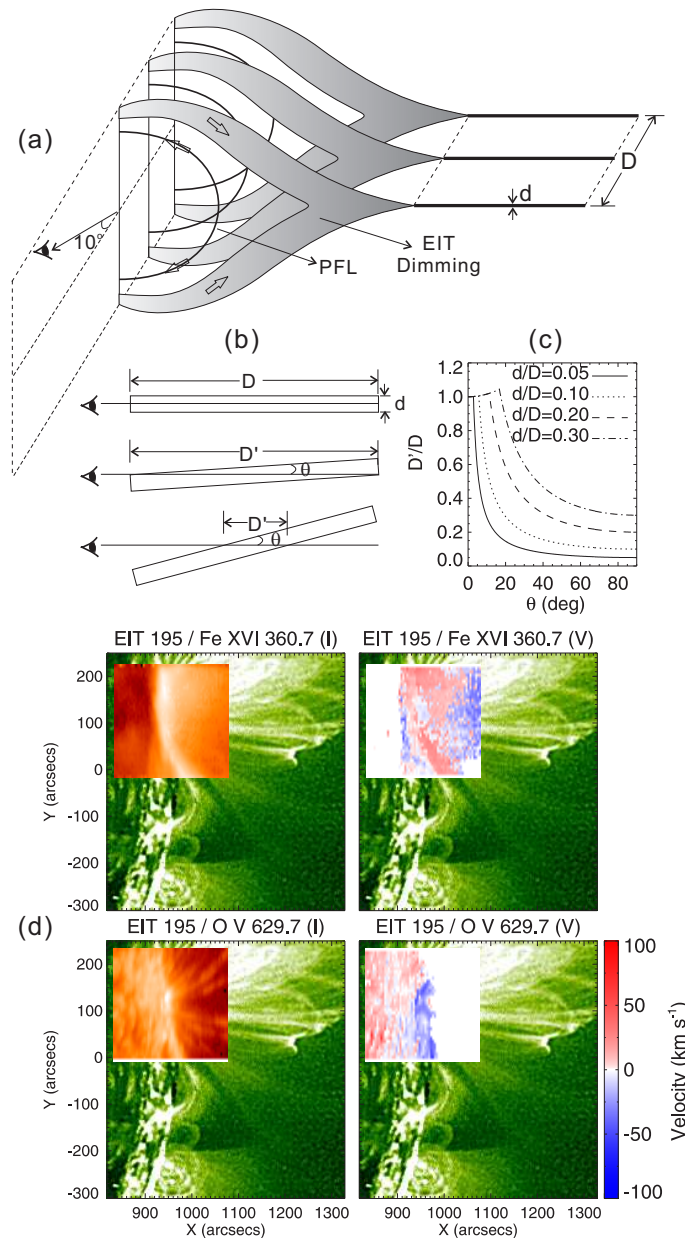


**Fig. 9** Upflow and downflow detected by CDS. (a) A schematic diagram illustrates the geometry of the reconnection region; (b) and (c) The change of the line-of-sight depth with the angle between the normal to the flare-loop plane and the line of sight; (d) EUV images of Fe 16 and O 5 and the corresponding velocity maps overlaid on the EIT 195 Å image taken at 13:32 UT.

Taking  $d/D = 0.1$ , for example,  $D'/D$  initially increases above 1 with  $\theta$ , reaches the maximum of 1.005 when  $\theta = 5.7^\circ$  and then decreases quickly to below  $e^{-1}$  for  $\theta > 16^\circ$  (Fig. 9(c)). Hence the current sheet is favorable for detection in a fairly narrow range of  $\theta$ . In this study,  $\theta$  is about  $10^\circ$ , which not only provides a line-of-sight emission measure large enough for the current sheet to be

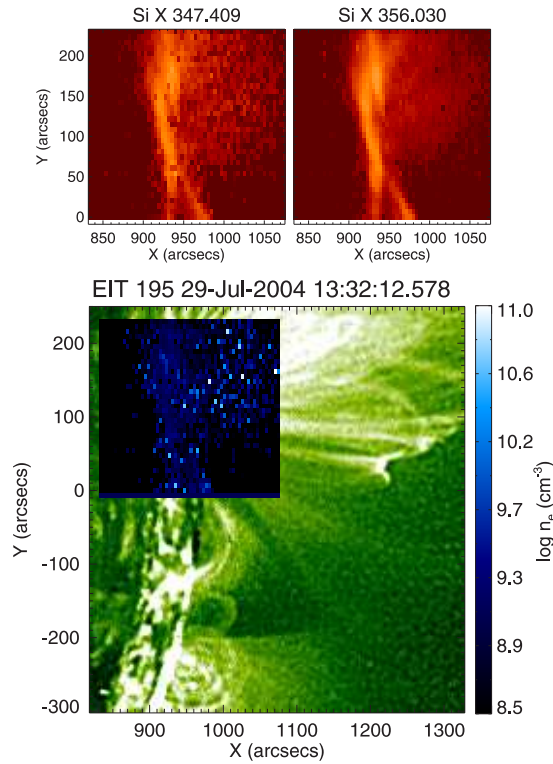


**Fig. 10** Density diagnosis using the density-sensitive Si 10 line pair. Top panels: images of Si 10 347.4 Å (*left*) and Si 10 356.0 Å (*right*); bottom panel: the density map obtained from the line ratio is overlaid on the EIT 195 Å image taken at 13:32 UT.

detected, but also allows for the detection of chromospheric evaporation (Sect. 2.5), an important consequence of magnetic reconnection in the corona.

As pointed out by Lin et al. (2009), the apparent thickness of the detected current sheet,  $d'$ , is also affected by the viewing angle, i.e.,  $d' = D \sin \theta + d \cos \theta$ . With  $\theta \approx 10^\circ$  and  $D \approx (7 \pm 1) \times 10^4$  km (Fig. 1),  $D \sin \theta = 1.2 \times 10^4$  km, which is larger than the observed thickness  $d' \approx (5\text{--}10) \times 10^3$  km (Fig. 3). This gives an estimation of the filling factor,  $f \approx 0.2\text{--}0.4$ , if we assume  $Df \sin \theta \approx d'/2$ .

### 3.2 Reconnection Rate

The rate of magnetic reconnection is characterized by the Alfvén Mach number,  $M_A$ , i.e., the ratio between the inflow speed and the Alfvén speed in the inflowing plasma. As a crude estimation, if we assume that the Alfvén speed in the inflowing plasma is comparable to that at the post-flare looptop (Sect. 2.2), then  $M_A = u_{\text{in}}/V_A \approx 0.007\text{--}0.013$ , where the inflow speed  $u_{\text{in}} \approx 4.2\text{--}7.6$  km s $^{-1}$  is measured in Section 2.3 (Fig. 4(e)) and  $V_A$  is about 600 km s $^{-1}$ . On the other hand, if we relate the observed blobs moving along the post-CME ray in LASCO/C2 (Fig. 6) to the reconnection outflow (Ko et al. 2003; Lin et al. 2005), then  $M_A = u_{\text{in}}/u_{\text{out}} \approx 0.01\text{--}0.02$  (Liu et al. 2010a), despite that the supposed outflow was not simultaneous with the inflow.

Alternatively, following Ko et al. (2003), we assume that the electromagnetic energy in the reconnection region is equally converted to the kinetic energy and the thermal energy, i.e.,

$$B^2/4\pi = 3nk_B T + n\mu m_p V_A^2/2,$$

where  $n$  is the plasma density. Hence,

$$V_A = \frac{B}{\sqrt{4\pi\mu m_p n}} = \sqrt{\frac{6k_B T}{\mu m_p}} = 198 \left( \frac{T}{1 \text{ MK}} \right)^{1/2} \text{ km s}^{-1}.$$

With  $T = 20 \text{ MK}$ , which is the formation temperature of Fe 24 ( $\lambda 192$ ), we get  $V_A = 880 \text{ km s}^{-1}$  and  $M_A \approx 0.005\text{--}0.009$ . The relatively slow reconnection rate may be manifested in SXR, whose lightcurve rises slowly and decays gradually (Fig. 4(f)). For a diffusion region of length  $L$  and width  $d$ ,  $d = L \times M_A \approx (3\text{--}7) \times 10^3 \text{ km}$ , with  $0.78 R_\odot < L \lesssim 1.05 R_\odot$  (Sect. 2.4.1) and  $M_A \approx 0.005\text{--}0.009$ , which is in agreement with the observed sheet thickness, i.e.,  $(5\text{--}10) \times 10^3 \text{ km}$  (Fig. 3).

In the spirit of an order-of-magnitude estimation, the Poynting flux of electromagnetic energy toward the current sheet,  $\mathcal{P}$ , due to merging from both sides of the Y-type current, is

$$\mathcal{P} = 2 \frac{B_{\text{in}}^2}{4\pi} u_{\text{in}} L D f \quad \text{erg s}^{-1},$$

where the magnetic field strength in the inflowing plasma,  $B_{\text{in}}$ , is unknown, the inflowing speed  $u_{\text{in}} \approx 6 \text{ km s}^{-1}$  (Sect. 2.3), the length of the current sheet  $L \approx 6 \times 10^{10} \text{ cm}$  (Sect. 2.4.1), the line-of-sight depth  $D \approx 7 \times 10^9 \text{ cm}$  (Sect. 2.2) and the filling factor  $f \approx 0.3$  (Sect. 3.1). Derived from *GOES* data, the peak radiative energy loss rate,  $\mathcal{P}_{\text{rad}}$ , is about  $2 \times 10^{26} \text{ erg s}^{-1}$  (Fig. 4(f)). Assuming  $\mathcal{P} \approx 2\mathcal{P}_{\text{rad}}$ , we get  $B_{\text{in}} \approx 6 \text{ G}$ . With  $E = |u_{\text{in}} B|$ , the electric field at the reconnection site is about  $3.6 \text{ V m}^{-1}$ . According to the empirical formula by Dulk & McLean (1978), the field strength of 6 G corresponds to a height of  $0.2 R_\odot$  (or 130 Mm) above the surface, which is approximately the height of the Y-point at 12:20 UT (Fig. 3(d) and Fig. 4(d)).

A long-standing question is whether the reconnection in the solar corona is of Petschek (1964) type, which features an X-type topology, or of Sweet-Parker (Sweet 1958; Parker 1957) type, which features a Y-type topology. The observed geometry in this study argues strongly for the latter. One may suggest that the observed sheet structure is due to a Petschek outflow that is directed upward above the X-point. In that case, one should also be able to see a similar structure due to the downward outflow, extending from the presumed X-point down to the flare looptop, where the downflow is deflected, such as the EUV “ridge” structure reported by Liu et al. (2009c) (see also Yokoyama & Shibata 2001, for an X-type geometry simulation). Because density decreases with height, the downward outflow should be more easily detected than its upward counterpart and its absence in EIT indicates that the upward outflow is not likely to be visible in EIT, either.

### 3.3 CME Initiation & Dynamics

The gradual expansion of the TLS was sustained for about 14 hours from 2004 July 28 21:08 UT to July 29 11:08 UT and by early July 29 ( $\sim 04:00 \text{ UT}$ ), the looptop had already risen beyond the EIT FOV. Liu et al. (2010b) studied 16 active-region coronal arcades within the EIT FOV, 12 of which evolved from post-eruptive arcades. Those arcades gradually expanded for several hours and suddenly erupted as CMEs, with the gradual expansion associated with significant helicity injection from the photosphere. Sheeley & Wang (2007) observed much higher coronal loops in the LASCO FOV, whose expansion was sustained for 1–2 days at  $\sim 20 \text{ km s}^{-1}$  and ended with the sudden formation of a pair of inward and outward components moving at speeds of  $\sim 100 \text{ km s}^{-1}$  and  $\sim 300 \text{ km s}^{-1}$ , respectively. Sheeley & Wang (2007) suggested that such “in/out pairs” result from a reconnection between closed loops of a rising arcade. The expansion of these loop systems may be driven by helicity injection (Fig. 2; see also Liu et al. 2010b), but the detailed mechanism leading up to the subsequent eruption could be complicated. Wang et al. (2002) studied a newly emerging twisted flux system which drives a slow reconnection in a bald patch between the overlying preexisting flux system and a TLS. The slow reconnection produces X-ray jets, removes the overlying flux and leads to a subsequent CME.

In our case, multiple jets can also be seen near the northern footpoints of the TLS during its gradual expansion (see the animation accompanying Fig. 3). Some jets apparently pumped material into the TLS. It is unclear whether the jets played a role in the subsequent eruption. Probably by loading mass into the TLS, more magnetic energy is allowed to be accumulated in the corona (Low 1999). The failure of the linear force-free extrapolation to reconstruct the TLS prior to eruptions may imply its nonlinear-force-free, or more likely, non-force-free nature. The expansion of the TLS was apparently accelerated from 11:08 UT onward, which sped up the convergence of the loop waist from  $\sim 1 \text{ km s}^{-1}$  to  $\sim 6 \text{ km s}^{-1}$  (Fig. 4(e)). By 12:06 UT, the CME already reached a speed of  $400 \text{ km s}^{-1}$  in LASCO C2. We speculate that via slow rising, the TLS may have reached an acceleration region where the TLS is too far from the Sun to be held back by its magnetic tension and therefore is carried away by the solar wind at hundreds of kilometers per second, as suggested by Sheeley & Wang (2007). With the CME propagation, the TLS was stretched to the point that the oppositely directed field lines at the waist were close enough to reconnect. Occurring in three dimensions, the reconnection may produce an outgoing helical flux rope, which manifests as a seemingly disconnected, twisted core structure in white light (e.g., Fig. 3(i)).

The dynamical evolution of the CME suggests that the dissipation of the current sheet may help to further accelerate the CME to speeds much higher than that of the solar wind originating from the equatorial region. The average CME speed in the C2 and C3 FOV, obtained via a linear fit, is  $429 \pm 17 \text{ km s}^{-1}$  and  $1306 \pm 21 \text{ km s}^{-1}$ , respectively. The overall height-time profile, however, is best fit by a cubic polynomial function (the red curve in Fig. 4(d)),  $h = a + bt + ct^2 + dt^3$ , with  $\chi_\nu^2 = 5.7^3$ , assuming the measurement error is 4 pixels in both C2 and C3. The acceleration of the CME decreased from  $\sim 320 \text{ m s}^{-2}$  at  $3 R_\odot$  at a rate of  $-3.6 \pm 0.2 \text{ cm s}^{-3}$ , and approached zero at about 14:36 UT at  $15 R_\odot$  (as indicated by the vertical line in Fig. 4(d)). Thus, we conclude that the current sheet was only under significant dissipation between about 11:30 (when radio DPSs started) and 14:36 UT, which is essentially the same time interval of the flare. The deceleration of the CME beyond  $15 R_\odot$  should mainly result from the interaction with the solar wind, since gravity ( $\propto r^{-2}$ ) is relatively negligible compared to magnetic forces ( $\propto r^{-1}$ ) beyond about two solar radii.

It has long been proposed that there are two dynamical types of CMEs (Gosling et al. 1976; MacQueen & Fisher 1983; Sheeley et al. 1999): 1) fast CMEs, which are accelerated impulsively in the low corona and decelerated in the coronagraph's FOV; and 2) slow CMEs, which are accelerated gradually in the coronagraph's FOV over a large height range. The CME observed here has a fast-CME speed, but undergoes a gradual acceleration between  $3 R_\odot$  and  $15 R_\odot$ , typical of a slow CME, which can be naturally attributed to the dissipation of the global-scale current sheet. The estimated reconnection rate (0.005–0.009) is consistent with the Lin & Forbes (2000) model, which requires that the reconnection rate be greater than 0.005 for high-speed ( $> 1000 \text{ km s}^{-1}$ ) CMEs.

#### 4 SUMMARY

The observed geometry of the reconnection region, i.e., the bright, collimated sheet extending above the cusp-shaped flaring loop, perfectly matches the standard picture for flares/CMEs (e.g., Kopp & Pneuman 1976; Lin & Forbes 2000). Significant implications of this observation have been discussed in Liu et al. (2010a). Summarized below are various dynamical features that are consistent with the reconnection scenario.

- The TLS waist converged at  $\sim 6 \text{ km s}^{-1}$  to a local area where the cusp-shaped flare loop subsequently formed. The argument by Chen et al. (2004) that the inflow pattern obtained by Yokoyama et al. (2001) was due to the rising of a reconnection X-point is irrelevant here, because the convergence (Fig. 4(e)) was observed prior to the formation of the flare loop and the Y-type current sheet.

---

<sup>3</sup>  $\chi_\nu^2$  is the standard deviation of the residuals, defined as  $\chi^2/N$ , where  $\chi^2$  is the chi-square estimator and  $N$  is the number of degrees of freedom.

- Radio DPSs were recorded during the flare rising phase, implying a fragmentation of the energy release occurred. The scales of dynamical processes could therefore be much smaller than the apparent scale of the sheet structure observed in EIT.
- A radio Type III burst occurred at the same time when the sheet structure as well as the cusp-shaped flare loop was clearly seen in EIT 195 Å, implying accelerated electrons were beaming upward from the upper tip of the current sheet.
- A cusp-shaped dimming in EIT was observed to be located above the post-flare arcade during the decay phase. Both the dimming and the arcade expanded with time, implying reconnection proceeded to higher and higher altitudes.
- The cusp-shaped dimming is associated with plasma upflows detected with CDS hot emission lines, while the post-flare arcade is associated with downflows detected with cold lines, implying the evaporation of heated chromospheric material and the precipitation of cooled coronal plasma respectively occurred.
- The current sheet orientation indicated by the cusp is approximately aligned with a white-light, post-CME ray, along which bright blobs suggestive of plasmoids were observed to move outward.
- The CME was propagating at  $\sim 400 \text{ km s}^{-1}$  when the current sheet was first detected in EUV and was continuously accelerated to speeds ( $\sim 1300 \text{ km s}^{-1}$ ) much faster than the solar wind originating from the equatorial region ( $\sim 400 \text{ km s}^{-1}$ ), which can be attributed to the dissipation of the global-scale current sheet.

**Acknowledgements** SOHO is a project of international cooperation between ESA and NASA. R.L., C.L., S.P. and H.W. were supported by NASA grants NNX08-AJ23G and NNX08-AQ90G and by NSF grant ATM-0849453. T.W. was supported by NASA grants NNX08AP88G and NNX09AG10G. J.L. was supported by NSF grant AST-0908344.

## Appendix A: CALCULATION OF HELICITY ACCUMULATION

We utilize MDI magnetograms to estimate the helicity accumulation in the relevant active region. We first apply the local cross-correlation tracking (LCT) method (November & Simon 1988) to estimate the change rate of relative magnetic helicity in an open volume through a boundary surface  $S$  (Chae et al. 2004; Chae & Jeong 2005), viz.,

$$\left(\frac{dH_m}{dt}\right)_{\text{LCT}} = -2 \int_S B_n (\mathbf{v}_{\text{LCT}} \cdot \mathbf{A}_p) dS,$$

where  $B_n$  is the magnetic field component normal to the surface  $S$ ,  $\mathbf{v}_{\text{LCT}}$  is the apparent horizontal velocity field component determined by the LCT technique and  $\mathbf{A}_p$  is the vector potential of the potential field under the Coulomb gauge, viz.,  $\hat{\mathbf{n}} \cdot \nabla \times \mathbf{A}_p = B_n$ ,  $\nabla \cdot \mathbf{A}_p = 0$  and  $\mathbf{A}_p \cdot \hat{\mathbf{n}} = 0$ . Here  $B_n$  can be estimated from the MDI line-of-sight field,  $B_l$ , viz.,  $B_l = B_n \cos \psi$ , where  $\psi$  is the heliocentric angle.  $\mathbf{A}_p$  is then calculated from  $B_n$  by using the fast Fourier transform method in a usual fashion. We perform LCT for all pixels with an absolute flux density greater than 5 G, but only those with cross correlation above 0.9 are used to obtain  $\mathbf{v}_{\text{LCT}}$  (for more details, see Park et al. 2008). The integration is carried out over the entire area of the target's active region. After the helicity change rate is determined as a function of time, we integrate it with respect to time to obtain the amount of helicity accumulation,

$$\Delta H_m = \int_{t_0}^t \left(\frac{dH_m}{dt}\right)_{\text{LCT}} dt,$$

where  $t_0$  and  $t$  are the start and end time of the helicity accumulation, respectively.

## References

- Antonucci, E., Alexander, D., Culhane, J. L., et al. 1999, in *The Many Faces of the Sun: a Summary of the Results from NASA's Solar Maximum Mission.*, eds. K. T. Strong, J. L. R. Saba, B. M. Haisch, & J. T. Schmelz, 331
- Aschwanden, M. J. 2002, *Space Sci. Rev.*, 101, 1
- Aschwanden, M. J., Kosugi, T., Hudson, H. S., Wills, M. J., & Schwartz, R. A. 1996, *ApJ*, 470, 1198
- Babcock, H. W. 1961, *ApJ*, 133, 572
- Bárta, M., Karlický, M., & Žemlička, R. 2008, *Sol. Phys.*, 253, 173
- Bemporad, A. 2008, *ApJ*, 689, 572
- Bemporad, A., Poletto, G., Suess, S. T., Ko, Y., Schwadron, N. A., Elliott, H. A., & Raymond, J. C. 2006, *ApJ*, 638, 1110
- Bougeret, J., Kaiser, M. L., Kellogg, P. J., et al. 1995, *Space Science Reviews*, 71, 231
- Brosius, J. W. 2006, *ApJ*, 636, L57
- Brueckner, G. E., Howard, R. A., Koomen, M. J., et al. 1995, *Sol. Phys.*, 162, 357
- Chae, J., & Jeong, H. 2005, *Journal of Korean Astronomical Society*, 38, 295
- Chae, J., Moon, Y., & Park, Y. 2004, *Sol. Phys.*, 223, 39
- Chen, P. F., Shibata, K., Brooks, D. H., & Isobe, H. 2004, *ApJ*, 602, L61
- Ciaravella, A., & Raymond, J. C. 2008, *ApJ*, 686, 1372
- Ciaravella, A., Raymond, J. C., Li, J., Reiser, P., Gardner, L. D., Ko, Y., & Fineschi, S. 2002, *ApJ*, 575, 1116
- Cox, A. N. 2001, *Allen's Astrophysical Quantities*, 4th edn., ed. Cox, A. N. (New York: Springer-Verlag)
- Delaboudinière, J., Artzner, G. E., Brunaud, J., et al. 1995, *Sol. Phys.*, 162, 291
- Dere, K. P., Landi, E., Mason, H. E., Monsignor Fossi, B. C., & Young, P. R. 1997, *A&AS*, 125, 149
- Drake, J. F., Swisdak, M., Che, H., & Shay, M. A. 2006, *Nature*, 443, 553
- Dulk, G. A., & McLean, D. J. 1978, *Sol. Phys.*, 57, 279
- Fisher, G. H., Canfield, R. C., & McClymont, A. N. 1985, *ApJ*, 289, 414
- Forbes, T. G. 2000, *J. Geophys. Res.*, 105, 23153
- Forbes, T. G., & Acton, L. W. 1996, *ApJ*, 459, 330
- Forbes, T. G., & Priest, E. R. 1995, *ApJ*, 446, 377
- Gosling, J. T., Hildner, E., MacQueen, R. M., Munro, R. H., Poland, A. I., & Ross, C. L. 1976, *Sol. Phys.*, 48, 389
- Handy, B. N., Acton, L. W., Kankelborg, C. C., et al. 1999, *Sol. Phys.*, 187, 229
- Harra, L. K., Matthews, S. A., & van Driel-Gesztelyi, L. 2003, *ApJ*, 598, L59
- Harrison, R. A., Sawyer, E. C., Carter, M. K., et al. 1995, *Sol. Phys.*, 162, 233
- Ji, H., Huang, G., & Wang, H. 2007, *ApJ*, 660, 893
- Ji, H., Huang, G., Wang, H., Zhou, T., Li, Y., Zhang, Y., & Song, M. 2006, *ApJ*, 636, L173
- Joshi, B., Veronig, A., Cho, K., Bong, S., Somov, B. V., Moon, Y., Lee, J., Manoharan, P. K., & Kim, Y. 2009, *ApJ*, 706, 1438
- Karlický, M., & Bárta, M. 2007, *A&A*, 464, 735
- Karpen, J. T., Antiochos, S. K., & Devore, C. R. 1995, *ApJ*, 450, 422
- Khan, J. I., & Hudson, H. S. 2000, *Geophys. Res. Lett.*, 27, 1083
- Khan, J. I., Vilmer, N., Saint-Hilaire, P., & Benz, A. O. 2002, *A&A*, 388, 363
- Kliem, B., Karlický, M., & Benz, A. O. 2000, *A&A*, 360, 715
- Ko, Y., Raymond, J. C., Lin, J., Lawrence, G., Li, J., & Fludra, A. 2003, *ApJ*, 594, 1068
- Kopp, R. A., & Pneuman, G. W. 1976, *Sol. Phys.*, 50, 85
- Kundu, M. R., Nindos, A., Vilmer, N., Klein, K., Shibata, K., & Ohyama, M. 2001, *ApJ*, 559, 443
- Lin, J., & Forbes, T. G. 2000, *J. Geophys. Res.*, 105, 2375
- Lin, J., Ko, Y., Sui, L., Raymond, J. C., Stenborg, G. A., Jiang, Y., Zhao, S., & Mancuso, S. 2005, *ApJ*, 622, 1251

- Lin, J., Li, J., Ko, Y., & Raymond, J. C. 2009, *ApJ*, 693, 1666
- Linker, J. A., Mikić, Z., Lionello, R., et al. 2003, *Phys. Plasmas*, 10, 1971
- Liu, R., Lee, J., Wang, T., Stenborg, G., Liu, C., & Wang, H. 2010a, *ApJ*, 723, L28
- Liu, R., Liu, C., Park, S., & Wang, H. 2010b, *ApJ*, 723, 229
- Liu, R., Wang, H., & Alexander, D. 2009a, *ApJ*, 696, 121
- Liu, W., Jiang, Y. W., Liu, S., & Petrosian, V. 2004, *ApJ*, 611, L53
- Liu, W., Petrosian, V., Dennis, B. R., & Holman, G. D. 2009b, *ApJ*, 693, 847
- Liu, W., Petrosian, V., Dennis, B. R., & Jiang, Y. W. 2008, *ApJ*, 676, 704
- Liu, W., Wang, T., Dennis, B. R., & Holman, G. D. 2009c, *ApJ*, 698, 632
- Liu, Y., Luhmann, J. G., Lin, R. P., Bale, S. D., Vourlidas, A., & Petrie, G. J. D. 2009d, *ApJ*, 698, L51
- Low, B. C. 1999, in *American Institute of Physics Conference Series* 471, eds. S. R. Habbal, R. Esser, J. V. Hollweg, & P. A. Isenberg, 109
- MacQueen, R. M., & Fisher, R. R. 1983, *Sol. Phys.*, 89, 89
- Masuda, S., Kosugi, T., Hara, H., Tsuneta, S., & Ogawara, Y. 1994, *Nature*, 371, 495
- McKenzie, D. E., & Hudson, H. S. 1999, *ApJ*, 519, L93
- Nakagawa, Y., & Raadu, M. A. 1972, *Sol. Phys.*, 25, 127
- Narukage, N., & Shibata, K. 2006, *ApJ*, 637, 1122
- November, L. J., & Simon, G. W. 1988, *ApJ*, 333, 427
- Park, S., Lee, J., Choe, G. S., Chae, J., Jeong, H., Yang, G., Jing, J., & Wang, H. 2008, *ApJ*, 686, 1397
- Parker, E. N. 1957, *J. Geophys. Res.*, 62, 509
- Petschek, H. E. 1964, *NASA Special Publication*, 50, 425
- Priest, E., & Forbes, T. 2000, *Magnetic Reconnection*, ed. Priest, E. & Forbes, T.
- Raymond, J. C., Ciaravella, A., Dobrzycka, D., Strachan, L., Ko, Y., Uzzo, M., & Raouafi, N. 2003, *ApJ*, 597, 1106
- Savage, S. L., McKenzie, D. E., Reeves, K. K., Forbes, T. G., & Longcope, D. W. 2010, *ApJ*, 722, 329
- Seehafer, N. 1978, *Sol. Phys.*, 58, 215
- Sheeley, N. R., Walters, J. H., Wang, Y.-M., & Howard, R. A. 1999, *J. Geophys. Res.*, 104, 24739
- Sheeley, Jr., N. R., & Wang, Y. 2007, *ApJ*, 655, 1142
- Shen, J., Zhou, T., Ji, H., Wang, N., Cao, W., & Wang, H. 2008, *ApJ*, 686, L37
- Shibata, K., Masuda, S., Shimojo, M., Hara, H., Yokoyama, T., Tsuneta, S., Kosugi, T., & Ogawara, Y. 1995, *ApJ*, 451, L83
- Stenborg, G., Vourlidas, A., & Howard, R. A. 2008, *ApJ*, 674, 1201
- Sui, L., & Holman, G. D. 2003, *ApJ*, 596, L251
- Sui, L., Holman, G. D., & Dennis, B. R. 2004, *ApJ*, 612, 546
- Sweet, P. A. 1958, in *IAU Symposium 6, Electromagnetic Phenomena in Cosmical Physics*, ed. B. Lehnert, 123
- Tripathi, D., Del Zanna, G., Mason, H. E., & Chifor, C. 2006, *A&A*, 460, L53
- Tsuneta, S. 1996, *ApJ*, 456, 840
- Tsuneta, S., Hara, H., Shimizu, T., Acton, L. W., Strong, K. T., Hudson, H. S., & Ogawara, Y. 1992, *PASJ*, 44, L63
- Veronig, A. M., Karlický, M., Vršnak, B., et al. 2006, *A&A*, 446, 675
- Wang, T., Sui, L., & Qiu, J. 2007, *ApJ*, 661, L207
- Wang, T., Yan, Y., Wang, J., Kurokawa, H., & Shibata, K. 2002, *ApJ*, 572, 580
- Webb, D. F., Burckpile, J., Forbes, T. G., & Riley, P. 2003, *Journal of Geophysical Research (Space Physics)*, 108, 1440
- Winterhalter, D., Smith, E. J., Burton, M. E., Murphy, N., & McComas, D. J. 1994, *J. Geophys. Res.*, 99, 6667
- Yokoyama, T., Akita, K., Morimoto, T., Inoue, K., & Newmark, J. 2001, *ApJ*, 546, L69
- Yokoyama, T., & Shibata, K. 2001, *ApJ*, 549, 1160
- Zarro, D. M., & Lemen, J. R. 1988, *ApJ*, 329, 456